Research Article

Unusually high corrosion resistance in Mo$_x$CrNiCo medium entropy alloy enhanced by acidity in aqueous solution

S. Shuang[a], G.J. Lyu[b,c], D. Chung[a], X.Z. Wang[d], X. Gao[a], H.H. Mao[e,f], W.P. Li[g], Q.F. He[a], B.S. Guo[h], X.Y. Zhong[g], Y.J. Wang[b,c], Y. Yang[a,g,i,*]

[a] Department of Mechanical Engineering, College of Engineering, City University of Hong Kong, Kowloon Tong, Kowloon, Hong Kong, China
[b] State Key Laboratory of Nonlinear Mechanics, Institute of Mechanics, Chinese Academy of Sciences, Beijing 100190, China
[c] School of Engineering Science, University of Chinese Academy of Sciences, Beijing 101408, China
[d] State Key Laboratory of Solidification Processing, Center of Advanced Lubrication and Seal Materials, Northwestern Polytechnical University, Xi'an 710072, China
[e] Unit of Structures, Department of Materials Science and Engineering, KTH, Stockholm SE-10044, Sweden
[f] Thermo-Calc Software, Råsundav. 18, Solna, SE-16767, Sweden
[g] Department of Materials Science and Engineering, College of Engineering, City University of Hong Kong, Kowloon Tong, Kowloon, Hong Kong, China
[h] Institute of Advanced Wear & Corrosion Resistant and Functional Materials, Jinan University, Guangzhou 510632, China
[i] Department of Advanced Design and System Engineering, College of Engineering, City University of Hong Kong, Kowloon Tong, Kowloon, Hong Kong, China

ARTICLE INFO

ABSTRACT

High corrosion resistance of alloys is essential for their structural applications; however, most alloys suffer from degradation of their corrosion resistance with the increasing acidity of their surroundings. Nonetheless, we developed a series of medium-entropy alloys (MEAs) in this work, which exhibit high strength, superior fracture toughness and ultra-high corrosion resistance, outperforming the variety of corrosion resistant alloys hitherto reported. Most interestingly, our MEAs exhibit an unusual anti-corrosion behavior and their corrosion resistance increases with acidity in Cl$^-$ containing solutions. Through extensive thermodynamic calculations, density functional theory (DFT) simulations and experiments, we reveal that the unusual anti-corrosion behavior of our MEAs can be attributed to their surface chemical complexity, which facilitates the physio-chemical-absorption of H$_2$O and O$_2$ and thus the rapid formation of metastable medium entropy passive films that contain the lowest amount of defects, as compared to the passive films on conventional alloys reported in the literature.

© 2023 Published by Elsevier Ltd on behalf of The editorial office of Journal of Materials Science & Technology.

1. Introduction

Metal corrosion has been a critical issue in a variety of engineering applications, which threatens the durability of structural components and could lead to expensive damage and even life loss if untendered [1]. Therefore, the development of corrosion resistant materials is pivotal and has been attracting tremendous research efforts over the past years [2]. Although various corrosion resistant alloys [3–5], such as stainless steels, Al alloys and Ti alloys, were developed following the conventional paradigm of alloy design [6], their corrosion resistance generally deteriorates with the increasing acidity in a harsh environment, which contains more aggressive species, such as chloride and hydrogen ions [4,7–9] ,

than in an ordinary solution (such as NaCl) with pH=7. On the other hand, the novel paradigm of "high entropy" alloy design eschews the conventional 'base element' notion, which has led to the discovery of numerous chemically complex alloys with outstanding mechanical or functional properties [10–13]. In this study, we demonstrate the ultra-high corrosion resistance in the Mo-Cr-Ni-Co medium-entropy alloy (MEA) even in Cl$^-$ containing low-pH solutions. Most importantly, unlike conventional corrosion resistant alloys, the corrosion resistance of the MEA becomes enhanced rather than deteriorated with the increasing acidity or reducing pH in the Cl$^-$ containing solution. Through a series of carefully designed electrochemical experiments and high-resolution transmission electron microscopy, we found that this unique behavior of our MEA can be attributed to the hydrogen ion assisted formation of a compact medium entropy passive film. Compared to the passive films reported in the literature, the medium entropy passive film is more stable and contains a very low point defect concen-

* Corresponding author at: Department of Mechanical Engineering, College of Engineering, City University of Hong Kong, Kowloon Tong, Kowloon, Hong Kong, China.
E-mail address: yonyang@cityu.edu.hk (Y. Yang).

tration and hydroxide/oxide ratio. Moreover, despite the abundance of Sigma phase (volume fraction > 10%) in the MEA, which is notorious for alloy embrittlement [14], our MEA displays a balanced combination of yield strength (~1.0 GPa) and room-temperature fracture toughness (~46 MPa m$^{0.5}$) [15]. These new discoveries may open up a vast space for the development of corrosion resistant alloys with an excellent combination of strength and toughness.

2. Experimental

2.1. Sample preparation

The Mo$_x$CrNiCo (x = 0.4, 0.6, 0.8, and 1.0) MEA samples were produced by arc melting pure (>99.9%) constituent metals under Ar atmosphere. To ensure chemical homogeneity, the alloy ingots were fully re-melted at least five times in a Ti-gettered argon atmosphere. The melt was subsequently cast into a water-cooled Cu mold (50 mm × 10 mm × 5 mm). Afterwards, all the MEA samples were cut into the geometry of 5 mm × 10 mm × 3 mm for electrochemical tests. Their surfaces were ground sequentially with SiC papers of up to 2500 grit and finally polished with 0.5 μm diamond powder. After that, these samples were cleaned with deionized water and alcohol, and dried in cold air. Prior to electrochemical measurements, the MEA samples were sealed in epoxy resin with only one exposed face of an area of 0.5 cm^2.

2.2. Microstructural analysis

Before the electrochemical tests, the microstructure and chemical composition of the samples were analysed by a scanning electron microscope (SEM, Quanta FEG450) equipped with energy dispersive X-ray spectrometry (EDS), and also by a transmission electron microscope (TEM, JEOL JEM-2100 F). In addition, X-ray diffraction (XRD, Rigaku SmartLab) using Cu K_α radiation was performed for phase identification.

2.3. Electrochemical corrosion measurements

The electrochemical tests were carried out in 1 mol/L Cl$^-$ solutions with different pH values (0, 2, 5, 7) at 25 °C under atmospheric pressure on the Vertex^{TM} electrochemical workstation (Iviumstat Technology). The concentration of Cl$^-$ and the pH for solutions were adjusted by NaCl and HCl. A typical three-electrode cell was utilized, which consisted of the test sample as the working electrode, a saturated calomel reference electrode (SCE), and a carbon rod counter electrode. All potentials stated in this work were measured against the SCE. The data of the open circuit potential (OCP) was recorded in a one-hour test to attain a steady value prior to the electrochemical tests. Potentiodynamic polarization tests were carried out at a rate of 1 mV/s from an initial potential of -0.3 V (vs. OCP) to a final potential of 1.3 V (vs. OCP). Growth of the passive film was monitored in situ using a single-frequency EIS (SF-EIS) method [16].

To probe the semi-conductive property, the capacitance of the passive film was measured in the anodic direction at a frequency of 1000 Hz using a 5 mV AC voltage and a scanning rate of 50 mV/s. Before the capacitance measurement, the electrodes were initially pre-passivated at OCP for 3 h. All the electrochemical tests were repeated at least 3 times to confirm the data reproducibility.

2.4. Characterization of the passive films and surface morphologies

To understand the mechanism of passivation, our samples were passivated for 10,000 s in the test solution at a potential of 0.40 V (vs. SCE) to obtain a stable passive film. Cross-section thin foils

containing the passive film were then prepared with the focused ion beam (FIB) technique (FEI Scios DualBeam). The TEM images of the passive films were obtained with the transmission electron microscope equipped with EDS. Moreover, the chemical composition of the passive films was inspected by XPS with an Al K_α radiation source. The binding energies of the XPS spectra were calibrated with the reference of adventitious C 1s peak (284.8 eV). The analyses of the narrow scan spectra were carried out by MultiPak and XPSPEAK 4.1 software by reference to NIST XPS database. To understand the mechanism of corrosion, the sample surface morphologies after the polarization test were examined using SEM.

2.5. CALPHAD

The Pourbaix diagrams for MEAs and 304 SS are calculated using Thermo-Calc software and a combination of thermodynamic databases. Three CALPHAD-based databases are applied here. They are TCAQ3, TCHEA4 and SSUB6. Among the databases the Gibbs energy for each phase is compatibly described as a function of composition, temperature and pressure. TCAQ3 includes the aqueous solution phase which consists of various anions, cations and neutral species. TCHEA4 includes metallic phases (e.g., FCC) for MEAs and 304 SS. The SSUB6 database includes the gas phase and all thermodynamically possible solid phases (e.g., oxides). The calculation results are presented in Pourbaix diagrams (i.e., Eh-pH diagrams), which shows the thermodynamic stability region of alloys and oxide precipitates in equilibrium with aqueous solution. The calculation conditions are at 25 °C, 1 atm, and 0.001 mole of alloys (MEAs or 304 SS) in 1 kg of H$_2$O with addition of 1 mole NaCl. The nominal compositions are used for MEAs and the composition for 304 SS is Cr$_{19.15}$Fe$_{73.31}$Ni$_{7.54}$ (at.%).

2.6. DFT simulations

A algorithm to construct Special Quasirandom Structure (SQS) implemented in ATAT code was used to generate the random solid solutions of dominated FCC phase of Mo0.6CrNiCo with totally 144 atoms [17]. The DFT calculation was performed with VASP [18]. A generalized-gradient-approximation (GGA) functional with Perdew-Burke-Ernzerhof (PBE) form was employed to describe the exchange-correlation potential. A Gamma-centered grid 4 × 3 × 1 k-point sampling was used for the surface calculation. A representative (001) plane was chosen to study the adsorption properties and a vacuum thickness of 15 Å was included to avoid surface-surface interaction. A 3 × 4 supercell was constructed with 6 atomic layers, with the bottom 3 atom layers being fixed for adsorption. The cutoff energy of plane-wave basis sets was set to 520 eV. An energy convergence criterion of 10^{-5} eV was set for the self-consistent field procedure and positions of ions were relaxed until a force convergence criterion of 0.02 eV/Å was reached. Spin polarization was not considered in all calculations. The visualizations of difference charge density were performed by VESTA [19].

3. Results and discussion

3.1. Microstructural characterization

Fig. 1(a) shows the X-ray diffraction (XRD) pattern of the as-cast Mo$_{0.6}$CrNiCo (at.%) MEA, which reveals that our MEA is composed of a face-centered cubic (FCC) and sigma (σ) phase. To characterize the microstructure, the surface of a specimen was chemically etched and examined under scanning electron microscopy (SEM). As seen in Fig. 1(b), a dual phase structure consistent with the XRD pattern could be observed. Based on our observations, the volume fraction of the FCC phase is estimated to be ~91% while the rest (~9%) is the σ phase. Transmission electron microscopy
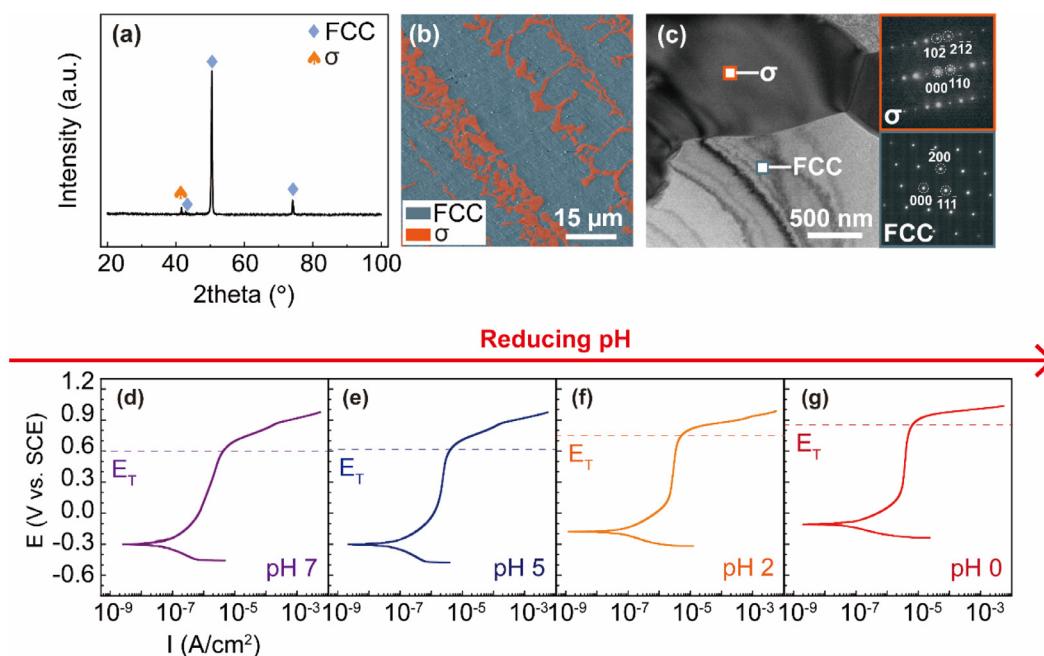
Fig. 1. Structure and electrochemical characterization of the $Mo_{0.6}CrNiCo$ medium entropy alloy (MEA). (a) XRD pattern of the as-cast $Mo_{0.6}CrNiCo$ MEA, (b) SEM image of the dual-phase (FCC and sigma phase) microstructure, (c) low magnification TEM image of the dual phase structure. The insets show the selected area electron diffraction pattern (SAED) of the sigma phase (upper panel) and FCC phase (lower panel). (d–g) Potentiodynamic polarization curves of the MEA in 1 mol/L Cl^- solution with different pH values.

(TEM) examination was also performed, which confirmed the crystalline structure of both phases through indexing the selected area electron diffraction (SAED) patterns (Fig. 1(c)), being consistent with the XRD result. The chemical compositions of the two phases were studied by energy dispersive spectroscopy (EDS), according to which the FCC phase is Mo-lean while the Laves phase is Mo-rich, as listed in Table S1 in the Supplementary Information.

3.2. Corrosion and passivation

In order to study the anti-corrosion behavior, potentiodynamic polarization curves of our MEA were measured in 1 mol/L Cl^- solution with a variety of pH values (Fig. 1(d–g)). In sharp contrast to 304 stainless steel (SS) (Fig. S1(a) in the Supplementary Information), our MEA exhibits an increasing transpassivation potential (E_T) with reducing pH, indicative of the formation of a more protective passive film in a more acidic environment [20]. After polarization tests, the corrosion morphologies of our MEA were examined with SEM, which reveals slightly selective corrosion in both the NaCl (pH= 7) (Fig. S1(b)) and HCl solution (pH=0) (Fig. S1(d)). In contrast, the surface of the 304 SS sample suffered from severe corrosion attack in both solutions (Fig. S1(c) and (e)).

Next, we extracted various key corrosion properties of our MEA from the polarization curves, including the corrosion potential E_{corr}, the corrosion current density I_{corr} and the transpassivation potential E_T, as listed in Table 1. Notably, our MEA exhibits a much nobler E_{corr} (-104 mV_{SCE}) in the HCl solution than in the NaCl solution (-292 mV_{SCE}) while retaining a steady I_{corr} value (between 3.92×10^{-8} and 5.53×10^{-8} A/cm^2) regardless of the pH of the solution, which is in sharp contrast to 304 stainless steel (SS), of which the corrosion current density rises by three orders of magnitude from 3.61×10^{-8} to 2.95×10^{-5} A/cm^2 as the pH of the solution reduces from 7 to 0 (Table S2). Furthermore, the E_T value of our MEA also increases, from 631 mV_{SCE} at pH = 7 to 883 mV_{SCE} at pH=0 in the Cl^- solution. For a comprehensive study, we compiled the corrosion properties of various corrosion resistant metals

Table 1
Corrosion properties of $Mo_{0.6}CrNiCo$ MEA samples obtained at room temperature in 1 mol/L Cl^- containing solutions with reducing pH.

pH	E_{corr} (mV_{SCE})	I_{corr} (A cm^{-2})	E_T (mV_{SCE})
7	-292 ± 14	$(3.92 \pm 0.65) \times 10^{-8}$	631 ± 12
5	-313 ± 12	$(5.32 \pm 0.30) \times 10^{-8}$	633 ± 12
2	-188 ± 7	$(5.23 \pm 0.36) \times 10^{-8}$	748 ± 22
0	-104 ± 24	$(5.53 \pm 0.57) \times 10^{-8}$	883 ± 7

[3,4,21–28] obtained in Cl^- solutions with different pH values at room temperature, which include elemental metals [21,22], steels [3,23,24], Mg alloys [25,26], Al alloys [4,27], and Cu alloy [28] (see Table 2 for details). Fig. 2(a) compares I_{corr} versus pH for the variety of alloys. As seen in Fig. 2(a), our MEA displays a remarkably low I_{corr} value which is seemingly insensitive to the pH of the solution. Nevertheless, there is a clear trend that the I_{corr} of other alloys increases, by one to three orders of magnitude, with reducing pH. Fig. 2(b) further compares E_T versus pH for different classes of passivating alloys. Evidently, the E_T of the MEA remains the highest relative to that of steels and Al alloys, and increases with reducing pH, which is opposite to the general trend shown by other alloys.

3.3. Passive film

To explore the mechanisms underpinning the superb corrosion resistance of our MEA, we constructed the Pourbaix diagram (electrochemical potential E versus pH) of the FCC (Fig. 3(a)) and sigma (Fig. 3(b)) phase through extensive calculations with CALPHAD following the literature [29]. As shown in Fig. 3(a) or (b), except for a small aqueous corrosion region #12, stable oxidization is predicted to take place by forming multicomponent oxides (e.g., Cr_2O_3, MoO_3) on the MEA throughout most of the E-pH space between two gas phases. This is in sharp contrast to the calculated

Table 2

Summary of the corrosion properties of corrosion resistant metal and alloys obtained at room temperature in Cl⁻ containing solutions with reducing pH. Note that the NaCl concentration (1 mol/L) in the testing solution for this study is equal to or higher than that for reported works. All the potentials listed in Table 2 were converted to the potentials versus standard calomel electrode (SCE).

Materials	Solution	pH	I_{corr} (A cm^{-2})	E_{corr} (mV$_{SCE}$)	E_T (mV$_{SCE}$)	Refs.
Mo$_{0.6}$CrNiCo	HCl+NaCl	7	3.92×10^{-8}	-292	631	This
	(1 mol/L Cl⁻)	5	5.32×10^{-8}	-313	633	study
		2	5.23×10^{-8}	-188	748	
		0	5.53×10^{-8}	-104	883	
Ti[a]	H$_2$SO$_4$+3.5 wt.%	2	1.10×10^{-6}	-700	-[b]	[21]
	NaCl	1.5	2.00×10^{-6}	-675		
		1	2.90×10^{-6}	-665		
		0.5	6.00×10^{-6}	-675		
		0.25	9.00×10^{-6}	-680		
Ni[a]	Britton Robinson	6	1.40×10^{-5}	-437	-[b]	[22]
	buffers	2	3.40×10^{-5}	-385		
Al[a]	Britton Robinson	6	1.60×10^{-5}	-547	-[b]	[22]
	buffers	2	1.00×10^{-4}	-757		
304 SS[c]	HCl+NaCl	7	3.61×10^{-8}	-185	255	This
	(1 mol/L Cl⁻)	5	7.14×10^{-8}	-164	223	study
		2	1.02×10^{-7}	-312	156	
		0	2.95×10^{-5}	-381	-[b]	
High strength pipeline steel	HCl+NaCl	7	2.64×10^{-5}	-700	-409	[3]
	(1 mol/L Cl⁻)	4	1.85×10^{-5}	-742	-562	
254SMO SS[c]	HCl+3.5 wt.% NaCl	5	8.60×10^{-8}	-256	920	[23]
		2	7.30×10^{-6}	-437	719	
		0.1	5.42×10^{-5}	-301	892	
Cr$_{23}$N$_{1.2}$ high nitrogen chromium steel	HCl+3.5 wt.% NaCl	6	7.86×10^{-7}	-354	278	[24]
		2	8.51×10^{-5}	-598	276	
		1	6.99×10^{-4}	-599	-181	
AZ63 Mg alloy	HCl+NaCl	8	9.15×10^{-4}	-1491	-[b]	[25]
	(1 mol/L Cl⁻)	3	1.10×10^{-3}	-1519		
		2	3.30×10^{-3}	-1619		
AZ91D Mg alloy	HCl+3.5 wt.% NaCl	7.25	6.82×10^{-4}	-1463	-[b]	[26]
		2	1.27×10^{-1}	-1688		
AA7075 Al alloy	H$_2$SO$_4$+0.05 mol/L	7	3.44×10^{-5}	-1010	-600	[4]
	NaCl	3	5.07×10^{-5}	-336	-278	
		0.85	2.01×10^{-3}	-621	-552	
AA7075 Al alloy coated with phenyltrimethoxysilane	H$_2$SO$_4$+0.05 mol/L NaCl	7	1.80×10^{-7}	-870	-555	[4]
		3	4.60×10^{-6}	-261	-192	
		0.85	4.00×10^{-6}	-369	-294	
7050-T7451 Al alloy	HCl+3.5 wt.% NaCl	4	5.34×10^{-4}	-1195.31	-[b]	[27]
		2	1.34×10^{-3}	-825.881		
		1	1.32×10^{-2}	-770.96		
CuCrZr	H$_2$SO$_4$+0.6 mol/L	7	4.3×10^{-2}	-190	-[b]	[28]
	NaCl	5	1.39×10^{-1}	-230		
		3	4.20×10^{-1}	-270		
		1	2.03	-290		

[a] Elemental metals.
[b] No passivation behaviour.
[c] Stainless steel.

Pourbaix diagram for the well-known corrosion resistant 304 SS, in which corrosion is predicted to occur when pH is smaller than 4.4 (Fig. S2). In addition, this difference could be attributed to that the MEA is able to form protective Mo oxides when the pH is low.

Subsequently, we studied the growth behaviour of the passive (oxide) films in real time by using single frequency electrochemical impedance spectroscopy (SF-EIS), which allowed us to calculate the thickness (h) of the oxide film as a function of time in different solutions (see Supplementary Information for details). As shown in Fig. 3(c), the passive film grew in HCl from 0.6 nm to a plateau value of ~3.3 nm within 20 s (average growth rate ~0.135 nm/s), while the passive film grew in NaCl from 0.2 nm to the plateau value ~8 nm within 350 s (average growth rate ~0.022 nm/s), which is about one-sixth slower than in HCl on average. Through cross-sectional TEM imagining (Fig. 3(d) and (g)), we examined the atomic structures of the passive films grown at the potential of +0.40 V$_{SCE}$ in 1 mol/L NaCl (Fig. 3(d)) and 1 mol/L HCl (Fig. 3(g)) for 3 h, respectively. According to our TEM images, the actual thickness of the passive film in NaCl is ~10 nm, about two times thicker than that (~4 nm) in HCl, which generally agrees with our SF-EIS predictions. Interestingly, owing to the different growth rates, the

passive film formed in NaCl exhibits a nanocrystalline (NC) FCC structure (Fig. 3(e)) while that in HCl is amorphous (Fig. 3(f)). According to Refs. [30,31], amorphous passive films are more corrosion resistant than crystalline passive films if their chemical compositions are similar.

To characterize the chemical composition of the passive films, we carried out a series of XPS experiments. As shown in Figs. 4 and 5, we were able to detect all constituent elements of our alloy in both passive films in the form of either oxide or hydroxide. We note that this behaviour is slightly different from the calculated Pourbaix diagrams (Fig. 3(a) and (b)) because the latter does not consider the kinetics in the formation of passive films [32]. Evidently, both passive films are rich in Cr and Mo but lean in Ni and Co (Fig. 6(a)). To be specific, the passive film in HCl comprises Cr^0, Cr$_{OX}^{3+}$, Cr$_{OH}^{3+}$, Mo^{4+} and Mo^{6+} while that in NaCl only comprises Cr^0, Cr$_{OH}^{3+}$, Mo^{4+} and Mo^{6+}. According to Ref. [33], Mo^{4+} corresponds to MoO$_2$ and Mo^{6+} to MoO$_4^{2-}$ in a passive film. Since MoO$_4^{2-}$ is more likely to form polymolybdate ions (e.g. Mo$_7$O$_{24}^{6-}$) as an insoluble product in an acidic environment, which effectively shields the chemical attack of corrosion species [34,35], it is desirable for a passive film to possess more Mo^{6+} to enhance its corro-
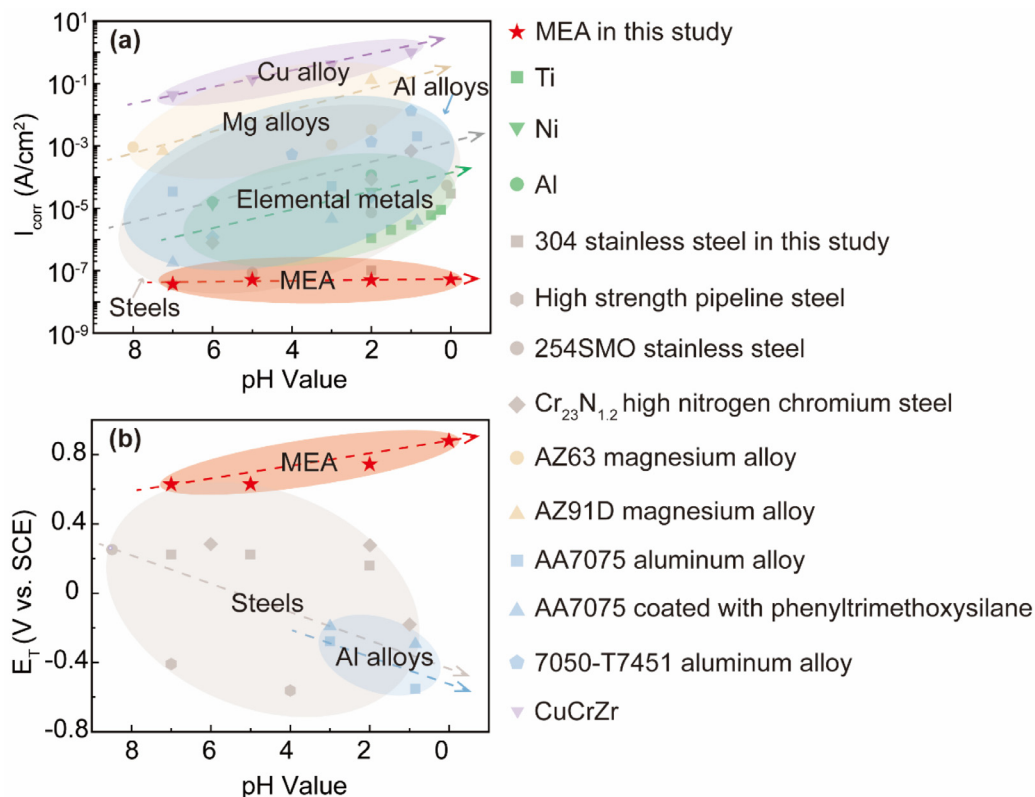
Fig. 2. Comparison of the corrosion properties of the $Mo_{0.6}CrNiCo$ MEA with other corrosion resistant alloys. The plots of (a) corrosion current density (I_{corr}) versus pH and (b) the transpassivation potential (E_T) versus pH.
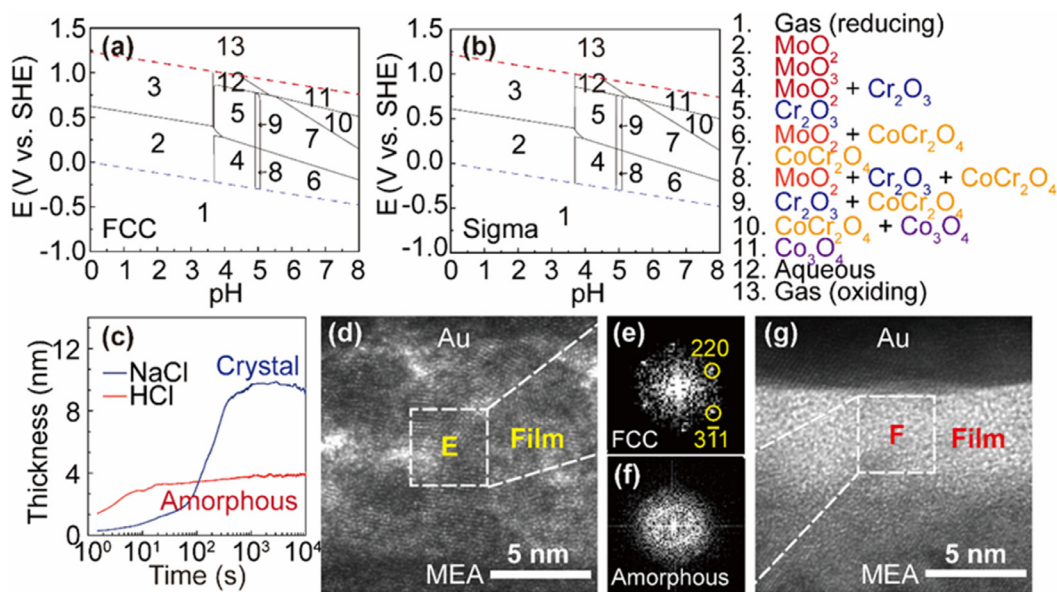

Fig. 3. Thermodynamic, kinetic and structural characterization of the passive film on the $Mo_{0.6}CrNiCo$ MEA. The calculated Pourbaix diagram for the FCC (a) and sigma (b) phases of $Mo_{0.6}CrNiCo$ MEA in 1 mol/L Cl^- containing solution. (c) Effective thickness of the passive film derived from the potentiostatic oxide growth tests on the MEA in NaCl or HCl. The cross-sectional HRTEM image of the passive film grown on the MEA in (d) 1 mol/L NaCl and (g) 1 mol/L HCl. (e) and (f) Fast Fourier Transformation (FFT) images of the passive film in (d) and (g), respectively. Note the red (blue) lines in Fig. 3(a) and (b) represent the boundaries between a non-gaseous phase and oxidizing (reducing) gas.

sion resistance. Notably, the molar ratio of Mo^{6+} to Mo^{4+} is 0.57 in the passive film formed in HCl as opposed to 0.45 in the passive film formed in NaCl, which supports the improved corrosion resistance of our alloy in HCl. Besides, we also note that the ratio of oxide to hydroxide (e.g. Ni and Co) is higher in the passive film in HCl than that in NaCl. This is consistent with our finding because

a higher oxide/hydroxide ratio usually suggests a better corrosion resistance of the passive film according to the literature [36,37]. Fig. 6(b) shows the XPS depth profiles of both passive films, from which it can be seen that the concentration of Cr near the surface of our MEA is greater than those of other metallic elements in both passive films.
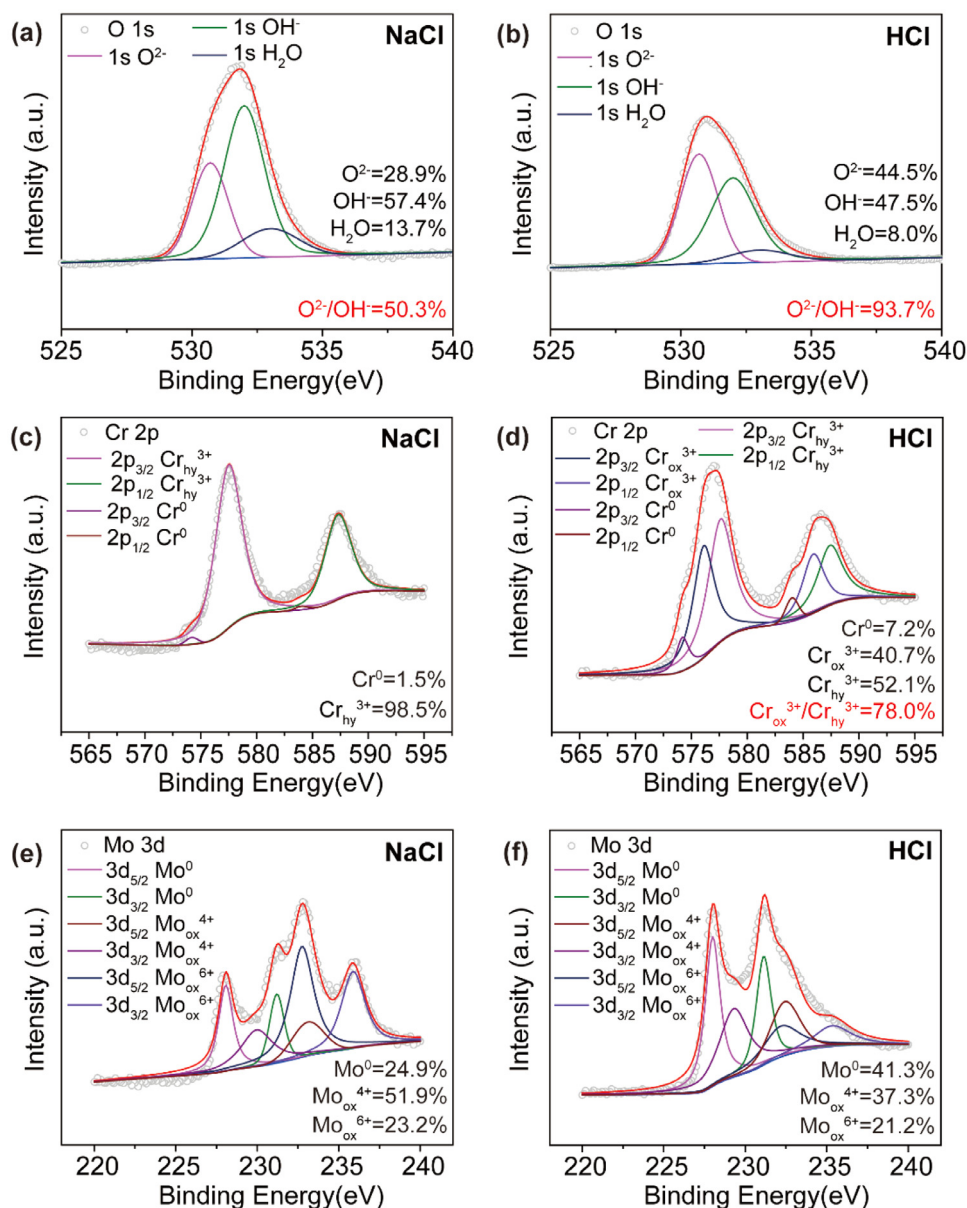
Fig. 4. Detailed XPS spectra of O 1s (a, b), Cr 2p (c, d) and Mo 5d (e, f) of the passive film formed on $Mo_{0.6}CrNiCo$ MEA in 1 mol/L NaCl and 1 mol/L HCl solutions.

Fig. S4(a) shows the Mott-Schottky (M-S) plots obtained from both passive films at the open circuit potential (OCP) in 1 mol/L NaCl solution for 3 h. Based on the well-established M-S relationship [38,39], we can calculate the level of point defects in both passive films. According to Fig. S4(a), we obtained the donor density $N_D= 2.6 \times 10^{20}$ cm^{-3} for the passive film formed in HCl and $N_D= 6.9 \times 10^{20}$ cm^{-3} for the one formed in NaCl. We further compared our results with the N_D values reported for a variety of corrosion resistant metals, as extracted from the M-S plots in low pH Cl$^-$ containing solutions (see Table S5 for details). As shown in Fig. 3(c), although all the prior results were obtained from solutions equally or less corrosive than ours (1 M HCl), the passive film formed on our MEA is characterized by the lowest N_D, which is about one to two orders of magnitude smaller than the N_D values hitherto reported for passive films formed on stainless steels [40–42], Ti alloy [43], Al alloys [44], Ni-Cr-Mo alloys [45], elemental metals [43,46] and metallic glass [47]. This extremely low defect concentration is strong evidence of the unusually high corrosion resistance of our MEA.

3.4. Absorption mechanism via first-principles calculations

Both the calculated Pourbaix diagrams and XPS results indicate that, aside from Cr, Mo plays a vital role in the passivation of our MEA. To elucidate the underpinning mechanisms, we performed extensive density functional theory (DFT) calculations to study the absorption of O_2/H_2O onto the surface of our MEA since it is generally accepted that O_2/H_2O absorption is critical to passive film formation [48]. In our DFT calculations, we chose a representative (001) plane and tested different adsorption sites (e.g. top, bridge and hollow sites). In general, our results indicate that the most stable adsorption sites for H_2O and O are the top and hollow sites, respectively. As shown in Fig. 7(a), the average adsorption energy is -0.53 ± 0.017 eV (physisorption) for H_2O. Compared to other constituent elements, Mo shows the strongest tendency for H_2O adsorption, which is followed by Cr, Co and Ni. Fig. 7(b) displays four different configurations of H_2O adsorption on top of the four different metallic atoms. For the adsorption of O atoms, we calculated 24 hollow- sites and classified the adsorption en-
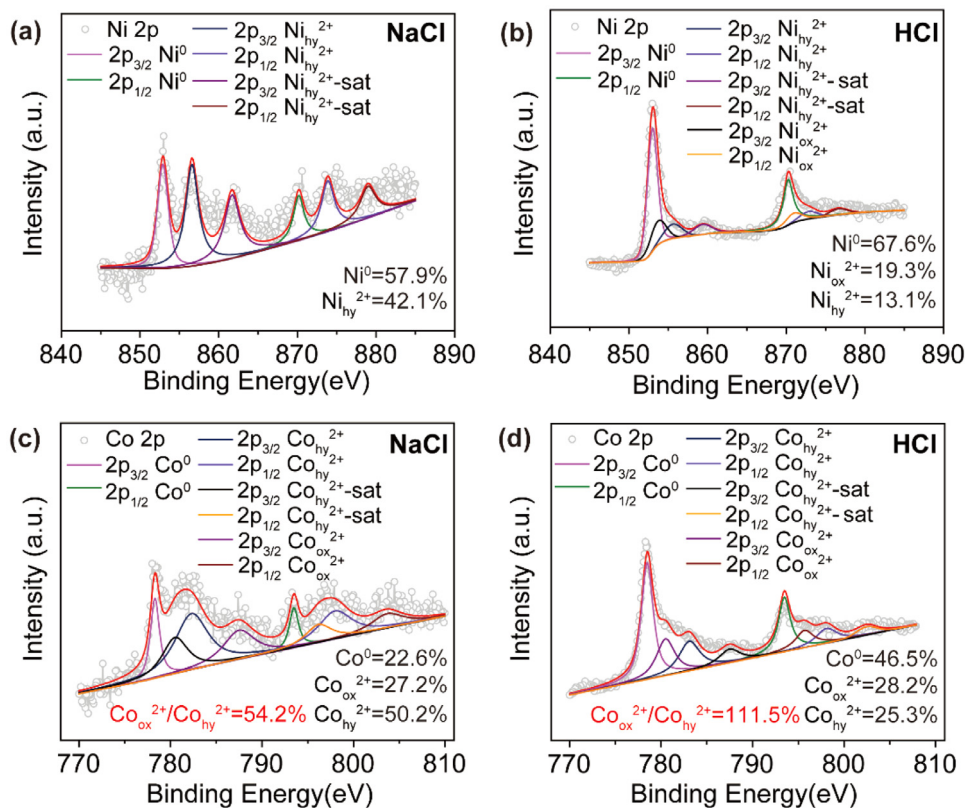
Fig. 5. Detailed XPS spectra of Ni 2p (a, b) and Co 2p (c, d) of the passive film formed on Mo$_{0.6}$CrNiCo MEA in 1 mol/L NaCl and 1 mol/L HCl solutions.
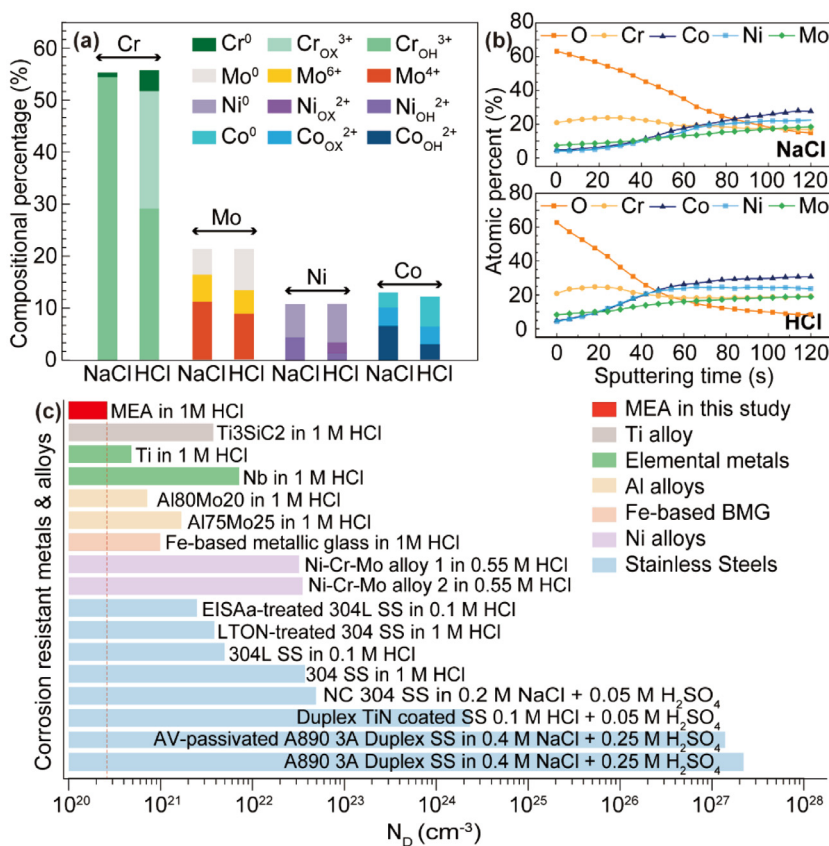

Fig. 6. Chemcial composition and defect density of the passive film on the Mo$_{0.6}$CrNiCo MEA. (a) Calculated cationic fractions of the passive films formed in NaCl and HCl solutions. (b) XPS depth profile (at.%) the elements in the passive films of the MEA after passivation in NaCl and HCl solutions. (c) Comparison of the donor density (N_D) of the passive films on the MEA with other passive films reported in the literature.
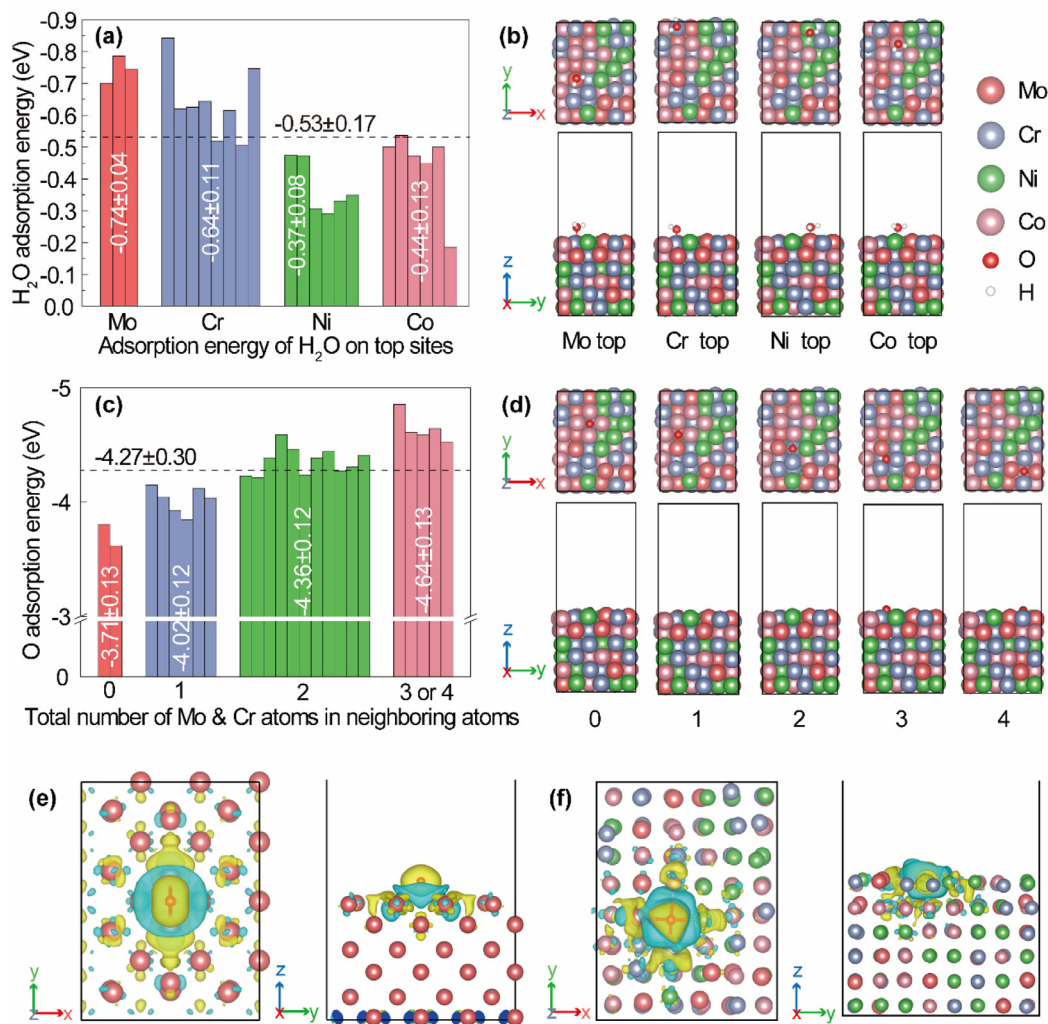
Fig. 7. DFT simulations of H_2O and O adsorptions on the MEA. Adsorption energy of (a) H_2O and (b) corresponding top-sites on four atoms with different types; adsorption energy of (c) O atom and (d) corresponding hollow-sites with different neighbouring atoms; the transfer of electron during the O adsorption on the surface of (e) (001) BCC-Mo and (f) (001) MEA.

ergy into four classes based on the total number of Mo and Cr as its neighbouring atoms in the top layer. As shown in Fig. 7(c), the average adsorption energy is -4.27 ± 0.3 eV (chemisorption) for O. Fig. 7(d) displays the typical adsorption configurations of O atoms with the varying number (0 to 4) of Mo and Cr as its neighbouring atoms. Evidently, more Mo or Cr atoms lead to stronger chemisorption of the O atoms. Electron density differences of O adsorptions on a simple BCC Mo and our MEA alloy were also calculated, which show the accumulation (yellow regions) and depletion (blue regions) of electrons during the adsorptions. Compared to the O adsorption on Mo (Fig. 7(e)), our MEA alloy (Fig. 7(f)) exhibits a more complex pattern of electron transfer, which demonstrates the complexity of our MEA in the adsorption process due to the chemical disorder. In addition, the more significant electron transfer around Mo and Cr atoms implies that Mo and Cr atoms are preferred during the O adsorption. Based on our DFT simulations, we conclude that, on one hand, Mo atoms in our MEA facilitate the physisorption adsorption of H_2O molecules and also provide the potential sites for the successive adsorption of O atoms; on the other hand, Mo and Cr atoms promote the chemisorption of O atoms. The combined actions of these constituent elements provide the synergy for the rapid formation of the excellent passive

film on the surface of our MEA, regardless of the acidity of the solution.
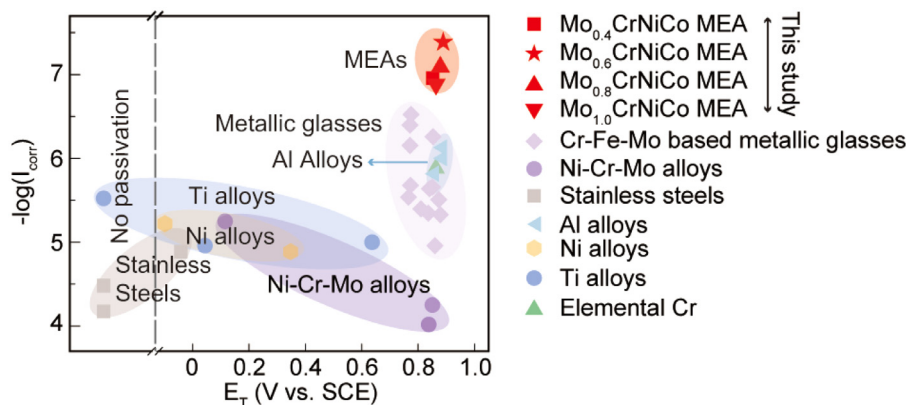
3.5. More corrosion resistant MEAs

Based on our above findings, we further extend the design of our MEA to include other possible corrosion-resistant compositions. Fig. S7(a) shows the XRD patterns of the as-cast $Mo_{0.4}CrNiCo$, $Mo_{0.8}CrNiCo$ and $Mo_{1.0}CrNiCo$, which all comprise an FCC and σ phase. As seen in the SEM images (Fig. S7(b-d)), the volume fraction of the σ phase increases with the Mo content. We performed potentiodynamic polarization tests on these MEAs in 1 mol/L HCl to characterize their anti-corrosion properties (Fig. S7(e)). We note that all the MEA samples passivated and exhibited remarkable anti-corrosion attributes (see Table 3 for details), which outperform many corrosion-resistant metals and alloys [49–58] (including other Ni-Cr-Mo alloys) in terms of $-log(I_{corr})$ and E_T, as clearly seen in Fig. 8. Moreover, we note that these MEAs also possess attractive mechanical properties, such as excellent hardness, good malleability, and superior fracture toughness [15], which are desirable for structural alloys.

Table 3

Summary of the corrosion properties of corrosion resistant metal and alloys obtained at room temperature in 1 mol/L HCl solution.

Materials	I_{corr} (A cm^{-2})	E_{corr} (mV$_{SCE}$)	E_T (mV$_{SCE}$)	Refs.
Mo$_{0.4}$CrNiCo	1.1×10^{-7}	-49	852	This study
Mo$_{0.6}$CrNiCo	5.5×10^{-8}	-104	883	
Mo$_{0.8}$CrNiCo	7.9×10^{-8}	-44	875	
Mo$_{1.0}$CrNiCo	1.3×10^{-7}	-57	865	
Cr$_{29.4}$Fe$_{29.4}$Mo$_{14.7}$C$_{14.7}$B$_{9.8}$Y$_2$ [a]	7.0×10^{-8}	-19	771	[49]
Cr$_{36.75}$Fe$_{22.05}$Mo$_{14.7}$C$_{14.7}$B$_{9.8}$Y$_2$ [a]	4.0×10^{-7}	-29	771	[49]
Cr$_{44.1}$Fe$_{14.4}$Mo$_{14.7}$C$_{14.7}$B$_{9.8}$Y$_2$ [a]	3.0×10^{-7}	-25	775	[49]
Fe$_{70}$Cr$_8$Mo$_2$P$_{13}$C$_7$ [a]	1.1×10^{-5}	-325	860	[50]
Fe$_{68}$Cr$_8$Mo$_4$P$_{13}$C$_7$ [a]	4.7×10^{-6}	-341	879	[50]
Fe$_{66}$Cr$_8$Mo$_6$P$_{13}$C$_7$ [a]	3.1×10^{-6}	-302	873	[50]
Fe$_{46}$Cr$_{16}$Mo$_{16}$C$_{18}$B$_4$ [a]	4.0×10^{-6}	-47	810	[59]
Fe$_{44}$Cr$_{16}$Mo$_{16}$C$_{18}$B$_6$ [a]	2.9×10^{-6}	-3	766	[59]
Fe$_{42}$Cr$_{16}$Mo$_{16}$C$_{18}$B$_8$ [a]	2.2×10^{-6}	-23	851	[59]
Fe$_{48}$Cr$_{15}$Mo$_{14}$C$_{15}$B$_6$Y$_2$ [a]	2.3×10^{-6}	-374	840	[60]
Fe$_{49}$Cr$_{15.3}$Mo$_{15}$Y$_2$C$_{15}$B$_{3.4}$N$_{0.3}$ [a]	5.5×10^{-7}	-7	853	[52]
Fe$_{43}$Cr$_{16}$Mo$_{16}$C$_{15}$B$_{10}$ [a]	4.5×10^{-6}	-54	836	[53]
Fe$_{43}$Cr$_{16}$Mo$_{16}$C$_{10}$B$_5$P$_{10}$ [a]	2.1×10^{-6}	-24	773	[53]
316L SS [b] coating	1.3×10^{-5}	-578	-41	[60]
304 SS [b]	3.3×10^{-5}	-384	-[c]	This study
SUS316 SS [b]	6.7×10^{-5}	-315	-[c]	[49]
Cr [d]	1.3×10^{-6}	-259	863	[61]
Al-36Cr-9Mo	7.3×10^{-7}	-80	880	[61]
Al-19Cr-25Mo	1.5×10^{-6}	-48	851	[61]
Al-26Cr-16Mo	9.8×10^{-7}	-70	880	[61]
Ni$_{59}$Zr$_{20}$Ti$_{16}$Si$_2$Sn$_3$	6.0×10^{-6}	-347	-98	[54]
Hastelloy B-2	5.0×10^{-6}	-51	97	[62]
HAYNES 282	5.6×10^{-5}	-250	858	[63]
INCONEL 718	9.6×10^{-5}	-272	845	[63]
Ni-19P	1.3×10^{-5}	-317	348	[55]
HT [e] Ti-Ni alloy CX1351-1A	1.1×10^{-5}	-237	44	[56]
Ti-31Al	1.0×10^{-5}	-742	637	[57]
Ti$_{45}$Zr$_5$Cu$_{45}$Ni$_5$	3.0×10^{-6}	-205	-[c]	[58]

[a] Metallic glasses.
[b] Stainless steels.
[c] No passivation behavior.
[d] Elemental metals.
[e] Heat treated.

Fig. 8. Comparison of the corrosion current density (I_{corr}) versus transpassivation potential (E_T) obtained from the Mo$_x$CrNiCo MEAs and other corrosion-resistant materials in 1 mol/L HCl at room temperature.

4. Conclusion

In summary, we developed a series of MEAs in this work with remarkably high corrosion resistance in chloride solution with pH ranging from 0 to 7. Unlike conventional alloys, the corrosion resistance of our MEAs is unusually improved with reducing pH in chloride solution. Such unique corrosion behaviour is due to the formation of a protective and compact medium entropy oxide film, which can be attributed to the synergic effect of the chemical complexity on absorption of H_2O and O_2. We note that, aside from the excellent corrosion resistance, these MEAs possess a balanced combination of yield strength, malleability and fracture toughness [15], which should have great potential as a structural alloy or a metallic coating for use in an extremely harsh environment.

Declaration of Competing Interest

Yong Yang, Shuo Shuang and Dukhyun Chung are inventors on a patent related to the alloy design described in this work. The rest of the authors declare no conflict of competing interest.

Acknowledgments

Supplementary materials

Supplementary material associated with this article can be found, in the online version, at doi:10.1016/j.jmst.2022.07.061.

References

[1] H. Luo, S.S. Sohn, W. Lu, L. Li, X. Li, C.K. Soundararajan, W. Krieger, Z. Li, D. Raabe, Nat. Commun. 11 (2020) 1–8.
[2] C.D. Taylor, P. Lu, J. Saal, G.S. Frankel, J.R. Scully, NPJ Mater. Degrad. 2 (2018) 6.
[3] Y. Wang, G. Cheng, W. Wu, Q. Qiao, Y. Li, X. Li, Appl. Surf. Sci. 349 (2015) 746–756.
[4] A. Younis, M.M.B. El-Sabbah, R. Holze, J. Solid State Electrochem. 16 (2012) 1033–1040.
[5] N. Dai, L.C. Zhang, J. Zhang, Q. Chen, M. Wu, Corros. Sci. 102 (2016) 484–489.
[6] Y.F. Ye, Q. Wang, J. Lu, C.T. Liu, Y. Yang, Mater. Today 19 (2016) 349–362.
[7] H. Sun, X. Wu, E.H. Han, Y. Wei, Corros. Sci. 59 (2012) 334–342.
[8] M. Karthega, S. Tamilselvi, N. Rajendran, Trends Biomater. Artif. Organs 20 (2006) 31–34.
[9] Y.Y. Chen, L.B. Chou, H.C. Shih, Mater. Sci. Eng. A 396 (2005) 129–137.
[10] Z. Lei, Y. Wu, J. He, X. Liu, H. Wang, S. Jiang, L. Gu, Q. Zhang, B. Gault, D. Raabe, Z. Lu, Sci. Adv. 6 (2020) 1–9.
[11] T. Yang, Y.L. Zhao, W.P. Li, C.Y. Yu, J.H. Luan, D.Y. Lin, L. Fan, Z.B. Jiao, W.H. Liu, X.J. Liu, J.J. Kai, J.C. Huang, C.T. Liu, Science 369 (2020) 427–432.
[12] Z. Jia, T. Yang, L. Sun, Y. Zhao, W. Li, J. Luan, F. Lyu, L.C. Zhang, J.J. Kruzic, J.J. Kai, J.C. Huang, J. Lu, C.T. Liu, Adv. Mater. 32 (2020) 1–9.
[13] Z.J. Chen, T. Zhang, X.Y. Gao, Y.J. Huang, X.H. Qin, Y.F. Wang, K. Zhao, X. Peng, C. Zhang, L. Liu, M.H. Zeng, J.B. Yu, Adv. Mater. 33 (2021) 2101845.
[14] C.-C. Hsieh, W. Wu, ISRN Metall. 2012 (2012) 732471.
[15] D.H. Chung, X.D. Liu, Y. Yang, J. Alloys Compd. 846 (2020) 156189.
[16] A.Y. Gerard, J. Han, S.J. McDonnell, K. Ogle, E.J. Kautz, D.K. Schreiber, P. Lu, J.E. Saal, G.S. Frankel, J.R. Scully, Acta Mater. 198 (2020) 121–133.
[17] A. Van De Walle, P. Tiwary, M. De Jong, D.L. Olmsted, M. Asta, A. Dick, D. Shin, Y. Wang, L.Q. Chen, Z.K. Liu, CALPHAD Comput. Coupling Phase Diagr. Thermochem. 42 (2013) 13–18.
[18] G. Kresse, J. Furthmüller, Comput. Mater. Sci. 6 (1996) 15–50.
[19] K. Momma, F. Izumi, J. Appl. Crystallogr. 44 (2011) 1272–1276.
[20] J. Soltis, Corros. Sci. 90 (2015) 5–22.
[21] N.T. Thomas, K. Nobe, J. Electrochem. Soc. 116 (1969) 1748–1751.
[22] B. Sefer, S. Virtanen, Corros. Sci. 150 (2019) 127–135.
[23] C.T. Liu, J.K. Wu, Corros. Sci. 49 (2007) 2198–2209.
[24] B. Tzaneva, J. Chem. Technol. Metall. 48 (2013) 383–390.
[25] R. Ambat, N.N. Aung, W. Zhou, J. Appl. Electrochem. 30 (2000) 865–874.
[26] H. Altun, S. Sen, Mater. Des. 25 (2004) 637–643.
[27] W.T. Tsai, J.B. Duh, J.J. Yeh, J.T. Lee, Y.C. Chang, Corrosion 46 (1990) 444–449.
[28] C.T. Kwok, P.K. Wong, H.C. Man, F.T. Cheng, J. Nucl. Mater. 394 (2009) 52–62.
[29] B. Zhang, Y. Zhang, S.M. Guo, J. Mater. Sci. 53 (2018) 14729–14738.
[30] B. Zhang, J. Wang, B. Wu, X.W. Guo, Y.J. Wang, D. Chen, Y.C. Zhang, K. Du, E.E. Oguzie, X.L. Ma, Nat. Commun. 9 (2018) 1–9.
[31] G. Okamoto, Corros. Sci. 13 (1973) 471–489.
[32] E. McCafferty, Introduction to Corrosion Science, Springer Science & Business Media, Germany, 2010.
[33] C.R. Clayton, Y.C. Lu, J. Electrochem. Soc. 133 (1986) 2465–2473.
[34] W.J. Tobler, S. Virtanen, Corros. Sci. 48 (2006) 1585–1607.
[35] J.D. Henderson, X. Li, D.W. Shoesmith, J.J. Noël, K. Ogle, Corros. Sci. 147 (2019) 32–40.
[36] C. Dai, H. Luo, J. Li, C. Du, Z. Liu, J. Yao, Appl. Surf. Sci. 499 (2020) 143903.
[37] H. Luo, Z. Li, A.M. Mingers, D. Raabe, Corros. Sci. 134 (2018) 131–139.
[38] G.A. Zhang, Y.F. Cheng, Electrochim. Acta 55 (2009) 316–324.
[39] A. Fattah-alhosseini, F. Soltani, F. Shirsalimi, B. Ezadi, N. Attarzadeh, Corros. Sci. 53 (2011) 3186–3192.
[40] Y.J. Jeong, S.J. Kim, Corros. Eng. Sci. Technol. 55 (2020) 217–223.
[41] L. Li, J. Wang, J. Yan, H. Fan, B. Zeng, X. Li, H. Dong, Metall. Mater. Trans. A–Phys. Metall. Mater. Sci. 51 (2020) 419–435.
[42] C. Pan, L. Liu, Y. Li, B. Zhang, F. Wang, J. Electrochem. Soc. 159 (2012) C453–C460.
[43] V.D. Jovic, M.W. Barsoum, J. Electrochem. Soc. 151 (2004) B71.
[44] M. Metikoš-Huković, R. Babić, Z. Grubač, J. Electrochem. Soc. 156 (2009) C435–C440.
[45] B. Yang, C. Shi, Y. Li, Q. Lei, Y. Nie, J. Mater. Res. 33 (2018) 3801–3808.
[46] D.G. Li, J.D. Wang, D.R. Chen, Electrochim. Acta 60 (2012) 134–146.
[47] H.X. Li, S.L. Wang, Y. Jeong, S. Yi, Int. J. Miner. Metall. Mater. 19 (2012) 726–732.
[48] H.Y.H. Chan, C.G. Takoudis, M.J. Weaver, J. Phys. Chem. B 103 (1999) 357–365.
[49] T. Xu, S. Pang, T. Zhang, J. Alloys Compd. 625 (2015) 318–322.
[50] M.W. Tan, E. Akiyama, A. Kawashima, K. Asami, K. Hashimoto, Corros. Sci. 38 (1996) 349–365.
[51] E. Akiyama, A. Kawashima, K. Asami, K. Hashimoto, Corros. Sci. 38 (1996) 1281–1294.
[52] J. Jayaraj, K.B. Kim, H.S. Ahn, E. Fleury, Mater. Sci. Eng. A 449-451 (2007) 517–520.
[53] S.J. Pang, T. Zhang, K. Asami, A. Inoue, Acta Mater. 50 (2002) 489–497.
[54] J. Jayaraj, D.J. Sordelet, D.H. Kim, Y.C. Kim, E. Fleury, Corros. Sci. 48 (2006) 950–964.
[55] H. Habazaki, S.Q. Ding, A. Kawashima, K. Asami, K. Hashimoto, A. Inoue, T. Masumoto, Corros. Sci. 29 (1989) 1319–1328.
[56] D. Starosvetsky, O. Khaselev, J. Yahalom, Corrosion 54 (1998) 524–530.
[57] Q. Yan, H. Yoshioka, H. Habazaki, A. Kawashima, K. Asami, Corros. Sci. 32 (1990) 327–335.
[58] S.J. Pang, H. Men, C.H. Shek, C. Ma, A. Inoue, T. Zhang, Intermetallics 15 (2007) 683–686.
[59] S.J. Pang, T. Zhang, K. Asami, A. Inoue, Corros. Sci. 44 (2002) 1847–1856.
[60] Z. Zhou, L. Wang, F.C. Wang, H.F. Zhang, Y.B. Liu, S.H. Xu, Surf. Coat. Technol. 204 (2005) 563–570.
[61] E. Akiyama, A. Kawashima, K. Asami, K. Hashimoto, Corros. Sci. 38 (1996) 279–292.
[62] J.J. Maurer, J.J. Mallett, J.L. Hudson, S.E. Fick, T.P. Moffat, G.A. Shaw, Electrochim. Acta 55 (2010) 952–958.
[63] L.O. Osoba, A.M. Oladoye, V.E. Ogbonna, J. Alloys Compd. 804 (2019) 376–384.